



---

# MiM-ISTD: MAMBA-IN-MAMBA FOR EFFICIENT INFRARED SMALL TARGET DETECTION

---

**Tianxiang Chen \***  
USTC, China  
Alibaba Cloud, China  
txchen@mail.ustc.edu.cn

**Zhentao Tan**  
USTC, China  
Alibaba Cloud, China  
tzt@mail.ustc.edu.cn

**Tao Gong**  
USTC, China  
tgong@ustc.edu.cn

**Qi Chu**  
USTC, China  
qchu@ustc.edu.cn

**Yue Wu**  
Alibaba Cloud, China  
matthew.wy@alibaba-inc.com

**Bin Liu**  
USTC, China  
flowice@ustc.edu.cn

**Jieping Ye**  
Alibaba Cloud, China  
yejieping.ye@alibaba-inc.com

**Nenghai Yu**  
USTC, China  
ynh@ustc.edu.cn

## ABSTRACT

Recently, infrared small target detection (ISTD) has made significant progress, thanks to the development of basic models. Specifically, the structures combining convolutional networks with transformers can successfully extract both local and global features. However, the disadvantage of the transformer is also inherited, i.e., the quadratic computational complexity to the length of the sequence. Inspired by the recent basic model with linear complexity for long-distance modeling, called Mamba, we explore the potential of this state space model for ISTD task in terms of effectiveness and efficiency in the paper. However, directly applying Mamba achieves poor performance since local features, which are critical to detecting small targets, cannot be fully exploited. Instead, we tailor a Mamba-in-Mamba (MiM-ISTD) structure for efficient ISTD. Specifically, we treat the local patches as "visual sentences" and use the Outer Mamba to explore the global information. We then decompose each visual sentence into sub-patches as "visual words" and use the Inner Mamba to further explore the local information among words in the visual sentence with negligible computational costs. By aggregating the word and sentence features, the MiM-ISTD can effectively explore both global and local information. Experiments on NUA-SIRST and IRSTD-1k show the superior accuracy and efficiency of our method. Specifically, MiM-ISTD is  $10\times$  faster than the SOTA method and reduces GPU memory usage by 73.4% when testing on  $2048 \times 2048$  image, overcoming the computation and memory constraints on high-resolution infrared images. Source code is available at <https://github.com/txchen-USTC/MiM-ISTD>.

**Keywords** Mamba-in-Mamba · State Space Model · Infrared Small Target Detection

## 1 Introduction

Infrared small target detection (ISTD) has been widely applied in remote sensing and military tracking systems. It is a binary segmentation task aiming to segment small target pixels from the background. The task is challenging because the targets are so small that present methods easily miss them or confound them with other background disturbances.

---

\*Work done as an intern at Alibaba Cloud.

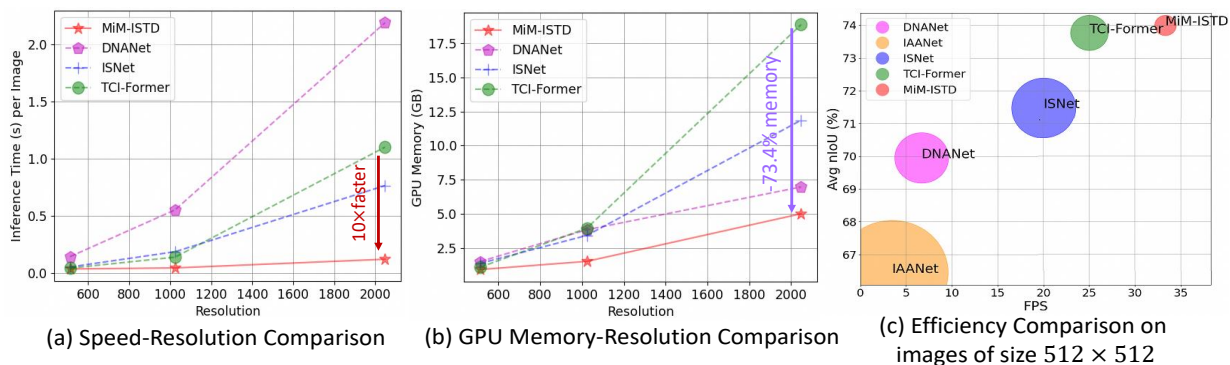


Figure 1: (a), (b) MiM-ISTD is more computation and memory efficient than present SOTA methods, DNANet [10] and TCI-Former [11], in dealing with high-resolution infrared images. Specifically, MiM-ISTD is 10× faster than TCI-Former [11] and saves 73.4% GPU memory per image with a resolution of 2048 × 2048. (c) The overall efficiency comparison on images of resolution 512 × 512, where larger bubbles denote higher GPU memory usage.

Present ISTD methods can be classified into traditional methods and deep-learning-based methods. In the early stages, traditional methods [1, 2, 3, 4, 5, 6, 7, 8, 9] take the dominance. However, these methods rely on prior knowledge and handcraft features, resulting in limited accuracy when applied to images that do not conform to their assumptions.

In recent years, deep-learning-based methods have significantly improved ISTD performances, and most of them are CNN-based methods [12, 13, 14, 15, 16, 17, 10, 18]. However, the drawback of CNN-based methods is that their focus on local features is at the cost of global contexts. Global contexts are important to ISTD because the background pixels and small targets often seem so similar that cannot be distinguished by local features alone, which easily triggers missed detection. As a solution, some hybrid methods [11, 19, 20, 21, 22, 23, 24] that combine ViT with CNN have been proposed to rely on ViT’s ability to model long-range dependencies. However, these methods generally suffer from a heavier computational burden due to the quadratic computational complexity of ViT. Despite certain work [19] adopting linear ViTs, its accuracy is still subordinate to the designs with quadratic complexity. Considering that high-resolution images are not rare in the infrared remote sensing domain (e.g. images produced by high-resolution infrared military sensors), this efficiency defect will be amplified when the resolution gets larger and hinder real-time ISTD. How to relieve the inefficiency while maintaining high ISTD accuracy is our main concern.

Recently, State Space Models (SSMs) have drawn increasing interest among researchers. Mamba [25] is the first proposed basic model built by SSMs and has achieved promising performance compared to booming transformers in various long-sequence modeling tasks while maintaining a linear complexity. In a short time, Mamba has achieved success in various fields [26, 27, 28, 29] and is considered to have the potential to become the next-generation basic model after transformers. However, when we directly transfer visual Mamba [28] to ISTD, the detection accuracy is not high, despite impressive model efficiency. The reason is that in ISTD the targets are typically very small, necessitating a greater emphasis on local features compared to other vision tasks that predominantly involve standard-size targets. Unfortunately, Mamba is not proficient in capturing these critical local features.

We aim to tailor a pure Mamba-based encoder to solve the locality defect while still maintaining a superior model efficiency. To this end, we get inspired by TNT [30], which effectively models local structural features with a trivial increase of computation and memory cost, and propose a novel Mamba-in-Mamba (MiM-ISTD) architecture for more efficient ISTD. To boost the feature representation ability of Mamba, we divide the input image into several patches as "visual sentences" and then further divide them into sub-patches as "visual words". We use an outer Mamba block to extract features of visual sentences, and further assist it with inner Mamba blocks to excavate the local features of smaller visual words. In particular, features and relations between visual words in each visual sentence are calculated independently using a shared network to ensure the added amount of parameters and FLOPs is minimal. Then, the visual word features are consolidated back into their respective sentences. In this way, MiM-ISTD enables us to extract visual information with refined granularity. We present in Figure 1 that MiM-ISTD exhibits superior efficiency over other methods in terms of GPU memory usage and inference time, particularly as the resolution of infrared images increases. In general, MiM-ISTD can achieve the most notable accuracy-efficiency balance compared with other SOTA methods.

Our contributions can be summarized in three folds:

- To the best of our knowledge, we are the first to apply Mamba to ISTD successfully, providing a new benchmark and valuable insights for future advancements in efficient and potent Mamba-based methods.
- To apply Mamba to the ISTD domain, we tailor a Mamba-in-Mamba (MiM-ISTD) structure in order to guarantee higher efficiency while sufficiently extracting both local and global information.
- Experiments on two public ISTD datasets, NUAAs-SIRST and IRSTD-1k, prove the superior accuracy and efficiency of our method. Specifically, MiM-ISTD achieves a speedup of 10 times over the SOTA while also cutting down GPU memory usage by 73.4% for each  $2048 \times 2048$  image during inference.

## 2 Related Work

### 2.1 Infrared Small Target Detection Networks

Generally speaking, present ISTD networks can be classified to two categories: CNN-based and hybrid networks. CNN-based networks mainly focus on local feature extraction. Dai et al. [16] propose asymmetric contextual modulation (ACM) for cross-layer information exchange to improve ISTD performance. They also design AlcNet [14], including a local attention module and a cross-layer fusion module to preserve the local features of small targets. Wang et al. propose MDvsFA [17], which applies generative adversarial network (GAN) to ISTD, and achieves a trade-off between miss detection and false alarm. BAUENet [13] introduces uncertainty to ISTD and achieves boundary-aware segmentation. DNANet [10] progressively interacts with high and low-level features. Dim2Clear [31] treats ISTD as an image detail reconstruction task by exploring the image enhancement idea. FC3-Net [32] explores feature compensation and cross-level correlation for ISTD task. ISNet [18] designs a simple Taylor finite difference-inspired block and a two-orientation attention aggregation module to detect targets.

Relying solely on local features for ISTD may lead to missed detection of small targets, which can merge into similar backgrounds and become indistinguishable. Therefore, hybrid methods complement local details with global contexts by combining ViT with CNN. IRSTFormer[33] adopts hierarchical ViT to model long-range dependencies but lays insufficient emphasis on mining local details. ABMNet [19] adopts ODE methods in both CNN and linear ViT structure design for ISTD. IAANet [20] concatenates local patch outputs from a simple CNN with the original transformer, but causes limited feature extraction, especially in low-contrast scenarios. RKformer [24] applies the Runge-Kutta method to build coupled CNN-Transformer blocks to highlight infrared small targets and suppress background interference. However, most of these hybrid methods suffer from a quadratic computational complexity due to the usage of ViT. Despite some work [19] adopting linear ViT design, its detection accuracy cannot be on par with other works with quadratic-complexity ViTs.

To improve network efficiency while maintaining high accuracy, we draw inspiration from both Mamba [25] and TNT [30], and propose a Mamba-in-Mamba architecture for ISTD, within which contains a pure Mamba-in-Mamba pyramid encoder that implements efficient local and global feature extraction.

### 2.2 Mamba in Vision Tasks

Recently, state space sequence models (SSMs) [26] have shown promise in efficiently handling long sequence modeling, offering an alternative for addressing long-range dependencies in visual tasks. Compared with transformers, SSMs are more efficient since they scale linearly with sequence length, and retain a superior ability to model long-range dependencies. Several latest studies have demonstrated the effectiveness of Mamba in vision tasks. For instance, Vim [34] proposed a generic vision backbones with bidirectional Mamba blocks. VMamba [28] proposed a hierarchical Mamba-based vision backbone and a cross-scan module to address the issue of direction-sensitivity arising from the disparities between 1D sequences and 2D image representations.

Notably, Mamba has been most widely applied to the medical image segmentation areas. U-Mamba [27], Vm-unet [35], Mamba-unet [36] and SegMamba [37] proposed a task-specific architecture with the Mamba block based on nnUNet [38], Swin-UNet [39], VMamba [28] and Swin-UNETR [40], respectively. P-Mamba [29] combined PM diffusion with Mamba to efficiently remove background noise while preserving target edge details. Swin-UMamba [41] verified that ImageNet-based pre-training is important to medical image segmentation for Mamba-based networks. Weak-Mamba-UNet [42] and Semi-Mamba-UNet [43] are for weak-supervised and semi-supervised medical image segmentation. Vivim [44] introduced Mamba for medical video object segmentation.

Since these Mamba models have achieved promising results in various vision tasks, we intend to study whether Mamba can also bring advancements to ISTD as it has brought to other vision tasks. However, when we directly apply visual Mamba blocks to ISTD, the detection accuracy is not considerable, despite superior model efficiency. The reason is that the targets in ISTD tasks are very small, which requires to pay more attention to the local features than other vision

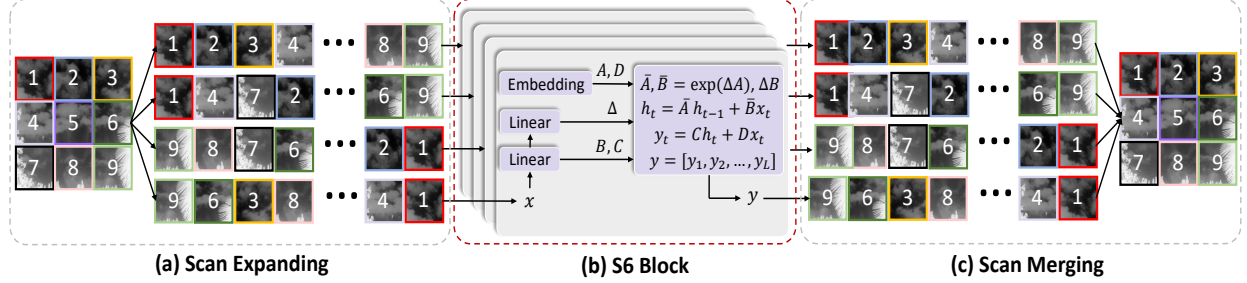


Figure 2: Illustration of the 2D Selective Scan (SS2D) on an infrared image. We commence by scanning an image using scan expanding. The four resulting feature sequences are then individually processed through the S6 block, and the four output sequences are merged (scan merging) to construct the final 2D feature map.

tasks with mainly common-size targets, while the original visual Mamba block cannot well explore these local features. To solve this defect, we propose Mamba-in-Mamba (MiM-ISTD) for ISTD, which takes visual sentences and visual words flows simultaneously and send each flows to respective visual Mamba blocks to obtain both local and global features with high efficiency.

### 3 Method

In this section, we describe our proposed Mamba-in-Mamba for efficient ISTD and analyze the computation complexity in detail.

#### 3.1 Preliminaries

##### 3.1.1 State Space Models.

State Space Models (SSMs) are commonly employed as linear time-invariant systems that transform a one-dimensional input stimulus  $x(t) \in \mathbb{R}^L$  through intermediary implicit states  $h(t) \in \mathbb{R}^N$  to an output  $y(t) \in \mathbb{R}^L$ . In mathematical terms, SSMs are typically described by linear ordinary differential equations (ODEs) (Equation 1), where the system is characterized by a set of parameters including the state transition matrix  $A \in \mathbb{C}^{N \times N}$ , the projection parameters  $B, C \in \mathbb{C}^N$ , and the skip connection  $D \in \mathbb{C}^1$ .

$$\begin{aligned} h'(t) &= Ah(t) + Bx(t) \\ y(t) &= Ch(t) + Dx(t) \end{aligned} \quad (1)$$

##### 3.1.2 Discretization.

State Space Models (SSMs) present significant challenges when applied to deep learning scenarios due to their continuous-time nature. To address this, the ODE needs to be transformed into a discrete function. Considering the input  $x_k \in \mathbb{R}^{L \times D}$ , a sampled vector within the signal flow of length  $L$  following [45], a timescale parameter  $\Delta$  can be introduced to the continuous parameters  $A$  and  $B$  into their discrete counterparts  $\bar{A}$  and  $\bar{B}$  following the zeroth-order hold (ZOH) rule. Consequently, Equation 1 can be discretized as follows:

$$\begin{aligned} h_k &= \bar{A}h_{k-1} + \bar{B}x_k \\ y(t) &= Ch(t) + Dx(t) \\ \bar{A} &= e^{\Delta A} \\ \bar{B} &= (e^{\Delta A} - I)A^{-1}B \\ \bar{C} &= C \end{aligned} \quad (2)$$

where  $B, C \in \mathbb{R}^{D \times N}$  and  $\Delta \in \mathbb{R}^D$ . In practice, we refine the approximation of  $\bar{B}$  using the first-order Taylor series:

$$\bar{B} = (e^{\Delta A} - I)A^{-1}B = (\Delta A)(\Delta A)^{-1}\Delta B = \Delta B \quad (3)$$

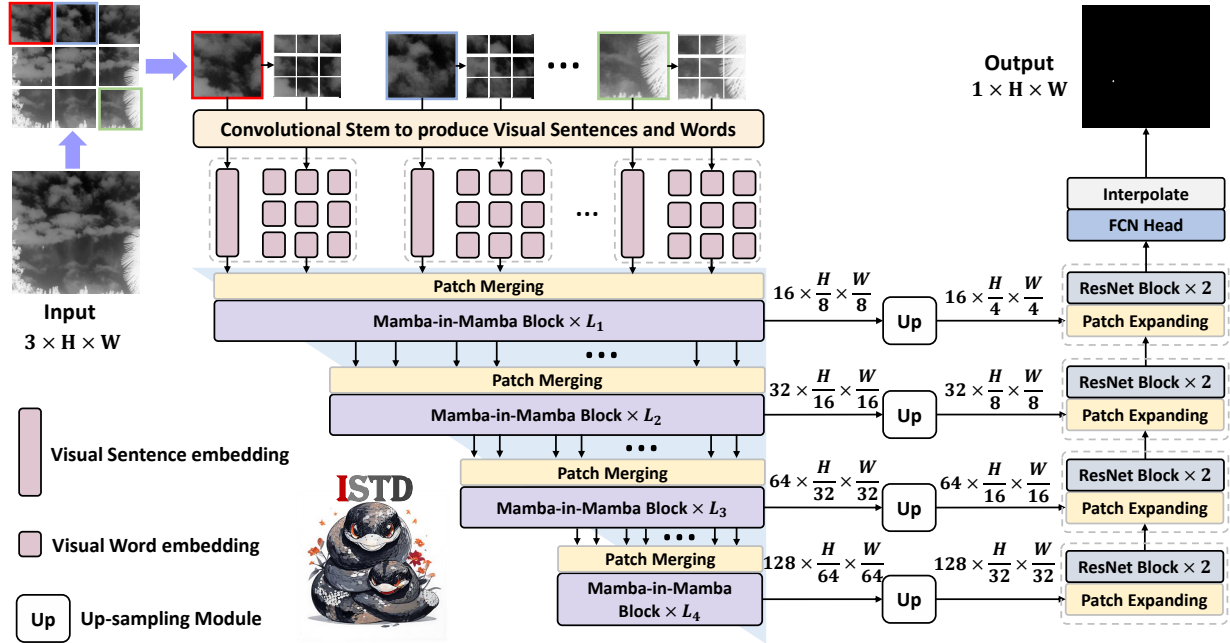


Figure 3: Overview of our MiM-ISTD, which mainly includes a convolutional stem, a pure Mamba-based MiM hierarchical encoder, and a plain decoder.

### 3.1.3 2D Selective Scan.

2D spatial information cannot be effectively captured by models designed for 1D data, making it unsuitable to directly apply Mamba to vision tasks. The 2D selective scan (SS2D) in [28] can address the issue. The overview of SS2D is depicted in Figure 2. SS2D arranges image patches in four different directions to generate four separate sequences. The quad-directional scanning strategy ensures that each element in the feature map integrates information from all other locations in different directions, thus creating a global receptive field without increasing linear computational complexity. Each resulting feature sequence is then processed using the selective scan space state sequential model (S6) before merging to reconstruct the 2D feature map. Given the input feature  $z$ , then the output feature  $\bar{z}$  of SS2D can be expressed as:

$$\begin{aligned}
 z_i &= \text{expand}(z, i) \\
 \bar{z}_i &= S6(z_i) \\
 \bar{z} &= \text{merge}(\bar{z}_1, \bar{z}_2, \bar{z}_3, \bar{z}_4)
 \end{aligned} \tag{4}$$

where  $i \in \{1, 2, 3, 4\}$  represents one of the four scanning directions.  $\text{expand}()$  and  $\text{merge}()$  refer to the scan expanding and scan merging operations in [28]. The S6 block in Equation 4 is the core SSM operator of SS2D. It enables each element in a 1D array to engage with any previously scanned samples through a condensed hidden state. For a more comprehensive understanding of S6, [28] provides an in-depth explanation.

## 3.2 Mamba-in-Mamba for Efficient ISTD

Present ISTD methods mainly typically employ CNNs or hybrids of CNNs and ViTs. The latter compensates for the shortcomings of the former in modeling long-range dependencies but suffers from a quadratic computational complexity. Recently, Mamba has been proposed. It is renowned for its superior model efficiency, less GPU memory usage, and better long-range dependency modeling and has been successfully applied to the vision domain. Therefore, we explore whether Mamba can also be applied to improve ISTD performances. However, when we directly apply visual mamba block to ISTD, the accuracy is not very impressive because local features, which matter a lot to detect small targets, are less explored. To address this deficiency, we propose a Mamba-in-Mamba (MiM-ISTD) architecture, shown in Figure 3, to learn both global and local information in an image while guaranteeing superb model efficiency.



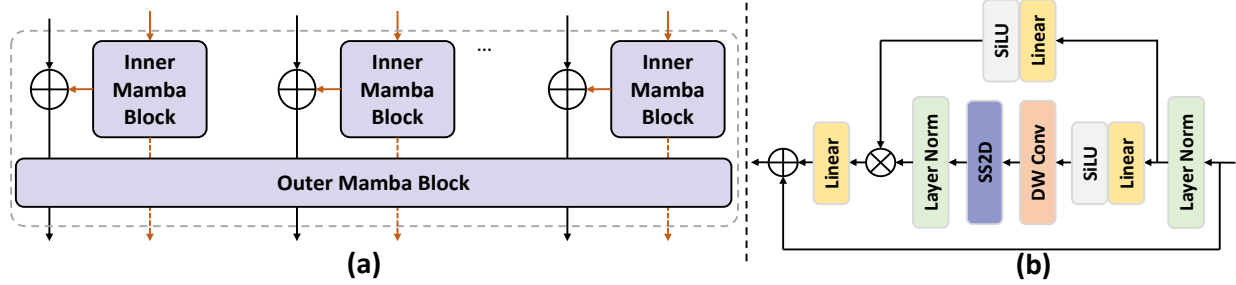


Figure 4: Overview of (a) our proposed Mamba-in-Mamba (MiM) block, which contains an inner Mamba block and an outer Mamba block, and (b) the visual Mamba block [28]. The inner Mamba block is shared in the same layer. The dashed line in (a) means bypassing the outer Mamba block.

Given a 2D infrared image  $\mathcal{X} \in \mathbb{R}^{H \times W \times 3}$ , it is divided evenly into  $n$  patches to form  $\mathcal{X} = [X^1, X^2, \dots, X^n]$  where each patch is in  $\mathbb{R}^{n \times p \times p \times 3}$ , with  $(p, p)$  denoting the resolution of each patch. In MiM-ISTD, we view the patches as visual sentences that represent the image. Further, each patch is segmented into  $m$  smaller sub-patches, making each visual sentence a sequence of visual words:

$$X^i = [x^{i,1}, x^{i,2}, \dots, x^{i,m}], j = 1, 2, \dots, m \quad (5)$$

where  $x^{i,j} \in \mathbb{R}^{s \times s \times 3}$  is the  $j$ -th visual word of the  $i$ -th visual sentence  $X^i$ ,  $(s, s)$  is the spatial size of sub-patches. Since our MiM adopts a hierarchical encoder structure, the spatial shapes of visual sentences and words are unfixed and will gradually decrease as the network layers deepen.

### 3.2.1 Convolutional Stem.

We construct a convolutional stem, where a stack of  $3 \times 3$  convolutions is utilized, to produce visual words  $\in \mathbb{R}^{\frac{H}{4} \times \frac{W}{4} \times C}$  and visual sentences  $\in \mathbb{R}^{\frac{H}{8} \times \frac{W}{8} \times D}$  at the first stage, where  $C$  is the visual word dimension and  $D$  is the visual sentence dimension. Each visual word corresponds to a  $2 \times 2$  pixel region in the original image, and each visual sentence is composed of  $4 \times 4$  visual words at this stage. Unlike ViTs, we do not add the position embedding bias to visual words and sentences due to the causal nature of visual mamba block [28].

### 3.2.2 MiM Hierarchical Encoder.

The core part of our MiM is its hierarchical encoder of four stages with different numbers of tokens, as shown in Figure 3. Across the four stages, the spatial shape of visual words is set as  $\frac{H}{2} \times \frac{W}{2}$ ,  $\frac{H}{4} \times \frac{W}{4}$ ,  $\frac{H}{8} \times \frac{W}{8}$  and  $\frac{H}{16} \times \frac{W}{16}$ . The spatial shape of visual sentences are set as  $\frac{H}{8} \times \frac{W}{8}$ ,  $\frac{H}{16} \times \frac{W}{16}$ ,  $\frac{H}{32} \times \frac{W}{32}$  and  $\frac{H}{64} \times \frac{W}{64}$ . We adopt the patch merging in [39] as the down-sampling operation. Each stage consists of multiple MiM blocks which process both word-level and sentence-level features. The visual words  $x^{i,j}$  are mapped to a sequence of word embeddings  $w^{i,j}$  via a linear projection, expressed as:

$$W^i = [w^{i,1}, w^{i,2}, \dots, w^{i,m}], w^{i,j} = FC(VEC(x^{i,j})) \quad (6)$$

where  $w^{i,j} \in \mathbb{R}^c$  is the  $j$ -th word embedding of the  $i$ -th visual sentence,  $c$  is the dimension of word embedding,  $W^i$  is the collection of word embeddings of the  $i$ -th visual sentence, and  $VEC()$  refers to the vectorization operation.

The MiM block handles two different data streams: one traverses through the visual sentences, while the other manages the visual words within each sentence. For the word embeddings, MiM block explores the relation between visual words:

$$W_l^i = W_{l-1}^i + Mamba(LN(W_{l-1}^i)), l = 1, 2, \dots, L \quad (7)$$

where  $l$  is the index of the  $l$ -th block, and  $L$  is the total count of such blocks. The first word embedding input  $W_0^i$  is the  $W^i$  in Equation 6. All transformed word embeddings are denoted by  $\mathcal{W}_l = [W_l^1, W_l^2, \dots, W_l^n]$ . This can be viewed as an inner Mamba block, illustrated in Figure 4(a). In this process, the relationships among visual words are built by computing interactions among each two visual words. For example, in a patch containing a small target, a word denoting the target would have a stronger relation with other target-related words while interacting less with the background part.

At the sentence level, we generate sentence embedding memories as storage for the sequence of sentence-level representations, initialized as zero:  $\mathcal{S}_0 = [S_0^1, S_0^2, \dots, S_0^n] \in \mathbb{R}^{n \times d}$ . In each layer, the sequence of word embeddings

is mapped to the domain of sentence embedding by linear projection and subsequently integrated into the sentence embedding:

$$S_{l-1}^i = S_{l-1}^i + FC(VEC(W_l^i)), l = 1, 2, \dots, L \quad (8)$$

By doing so, the sentence embedding can be augmented by the word-level features. We use another Mamba block, denoted as outer Mamba block, to transform the sentence embeddings:

$$S_l = S_{l-1} + Mamba(LN(S_{l-1})), l = 1, 2, \dots, L \quad (9)$$

The outer Mamba block can model the relationships among sentence embeddings. The inputs and outputs of the MiM block are visual word embeddings and sentence embeddings, so the MiM hierarchical encoder can be defined as

$$W_l, S_l = MiM(W_{l-1}, S_{l-1}), l = 1, 2, \dots, L \quad (10)$$

In our MiM block, both the inner Mamba block and the outer Mamba block adopt the visual mamba block [28], as shown in Figure 4 (b). The inner Mamba block models the relationship between visual words for local feature extraction, while the outer Mamba block captures the global feature by modelling the relationship between visual sentences. We set the block number  $L_1, L_2, L_3, L_4 = 2, 4, 9, 2$  of each stage by default. Stacking the MiM blocks for  $L = 17$  layers, we build our MiM hierarchical encoder.

We feed the visual sentence embedding outputs of each stage to the respective decoder stages. The spatial shapes of the four-stage encoder outputs are  $\frac{H}{8} \times \frac{W}{8}, \frac{H}{16} \times \frac{W}{16}, \frac{H}{32} \times \frac{W}{32}$  and  $\frac{H}{64} \times \frac{W}{64}$ , which are different from the feature map scales from typical backbones. To solve this discrepancy, these outputs should pass through straightforward up-sampling modules before reaching the decoder. The module includes a  $2 \times 2$  transposed convolution with a stride of two, succeeded by batch normalization [46], GeLU [47], a stride-one  $3 \times 3$  convolution, another batch normalization and GeLU. Therefore our MiM hierarchical encoder can produce feature maps with strides of 4, 8, 16, and 32 pixels relative to the input image.

### 3.2.3 Decoder Structure.

In contrast to the patch merging [39] operation used in the encoder for down-sampling, we use the patch expanding layer [39] in the decoder for up-sampling. In each decoder stage, we integrate the up-sampled encoder outputs with the expanded decoder features and send the integrated feature to basic ResNet blocks. Finally, the features go through a fully connection network head and an interpolation operation to get the final mask prediction.

### 3.2.4 Complexity Analysis.

Given a visual sequence  $T \in \mathbb{R}^{1 \times n \times d}$ , the computation complexity of SSM is  $8ndN$  [34], where  $N$  is the SSM dimension and is set to 16 by default. For simplicity, we only consider the core SSM in SS2D and 3 linear layers and calculate the FLOPs of a visual Mamba block as  $8ndN + 3nd^2$ . The MiM block includes an inner Mamba block, an outer Mamba block, and a linear layer, with complexities of  $8mncN + 3mnc^2, 8ndN + 3nd^2$ , and  $nmcd$ , where  $m$  is the number of visual words in a visual sentence and  $c$  is the word embedding dimension. Thus, the total FLOPs for the MiM block  $FLOPs_{MiM}$  sum to  $8mncN + 8ndN + 3mnc^2 + 3nd^2 + nmcd$ , still maintaining a linear complexity. While the FLOPs of the standard transformer block  $FLOPs_{ST}$  is  $2nd(6d + n)$  [30]. Considering that  $c \ll d$  and  $m \ll n$  in high resolution infrared images, the ratio of  $FLOPs_{MiM}$  and  $FLOPs_{ST}$  approaches 0, meaning that our MiM block introduces a trivial FLOP increase while offering a superior accuracy-efficiency balance demonstrated in subsequent experiments.

## 4 Experiments

### 4.1 Experimental Settings

#### 4.1.1 Datasets.

We choose NUAA-SIRST [16] and IRSTD-1k [18] as benchmarks for training, validation, and testing. NUAA-SIRST contains 427 infrared images of various sizes while IRSTD-1k consists of 1,000 real infrared images of  $512 \times 512$  in size. We resize all images of NUAA-SIRST to size  $512 \times 512$  for training and testing. IRSTD-1k is a more difficult ISTD dataset with richer scenarios. For each dataset, we use 80% of images as the training set and 20% as the test set.

#### 4.1.2 Evaluation Metrics.

We compare our method with other SOTA methods in terms of both pixel-level and object-level evaluation metrics. The pixel-level metrics include Intersection over Union ( $IoU$ ) and Normalized Intersection over Union ( $nIoU$ ), while the object-level metrics include Probability of Detection ( $P_d$ ) and False-Alarm Rate ( $F_a$ ).

Table 1: Accuracy comparison on NUAA-SIRST and IRSTD-1k. The figures in bold and underline mark the highest and the 2nd highest ones in each column.

Method	Type	NUAA-SIRST				IRSTD-1k			
		IoU $\uparrow$	nIoU $\uparrow$	Pd $\uparrow$	Fa $\downarrow$	IoU $\uparrow$	nIoU $\uparrow$	Pd $\uparrow$	Fa $\downarrow$
PSTNN [6]	Trad	22.40	22.35	77.95	29.11	24.57	17.93	71.99	35.26
MSLSTIPT [4]	Trad	10.30	9.58	82.13	1131	11.43	5.93	79.03	1524
MDvsFA [17]	CNN	60.30	58.26	89.35	56.35	49.50	47.41	82.11	80.33
ACM [16]	CNN	72.33	71.43	96.33	9.325	60.97	58.02	90.58	21.78
AlcNet [14]	CNN	74.31	73.12	97.34	20.21	62.05	59.58	92.19	31.56
DNANet [10]	CNN	75.27	73.68	98.17	13.62	69.01	66.22	91.92	17.57
Dim2Clear [31]	CNN	77.20	75.20	99.10	6.72	66.3	64.2	93.7	20.9
FC3-Net [32]	CNN	74.22	72.64	99.12	6.569	64.98	63.59	92.93	15.73
IAANet [20]	Hybrid	75.31	74.65	98.22	35.65	59.82	58.24	88.62	24.79
RKformer [24]	Hybrid	77.24	74.89	99.11	<b>1.580</b>	64.12	64.18	93.27	18.65
ISNet [18]	CNN	80.02	78.12	99.18	4.924	68.77	64.84	95.56	15.39
TCI-Former [11]	Hybrid	80.79	79.85	<u>99.23</u>	4.189	70.14	67.69	<u>96.31</u>	14.81
MiM-ISTD	Mamba	<b>80.80</b>	<b>80.20</b>	<b>100</b>	<u>2.179</u>	<b>70.33</b>	<b>67.82</b>	<b>96.91</b>	<b>13.49</b>

$IoU$  measures the accuracy of detecting the corresponding object in a given dataset.  $nIoU$  is the normalization of  $IoU$ , which can make a better balance between structural similarity and pixel accuracy of infrared small targets.  $IoU$  and  $nIoU$  are defined as:

$$IoU = \frac{A_i}{A_u}, nIoU = \frac{1}{N} \sum_{i=1}^N \left( \frac{TP[i]}{T[i] + P[i] - TP[i]} \right), \quad (11)$$

where  $A_i$  and  $A_u$  are the areas of intersection and union region between the prediction and ground truth, respectively.  $N$  is the total number of samples,  $TP[\cdot]$  is the number of true positive pixels,  $T[\cdot]$  and  $P[\cdot]$  is the number of ground truth and predicted positive pixels.

$P_d$  calculates the proportion between the number of correctly predicted targets  $N_{pred}$  and all targets  $N_{all}$ .  $F_a$  refers to the ratio of falsely predicted target pixels  $N_{false}$  and all the pixels in the infrared image  $N_{all}$ .  $P_d$  and  $F_a$  are calculated as follows:

$$P_d = \frac{N_{pred}}{N_{all}}, F_a = \frac{N_{false}}{N_{all}}. \quad (12)$$

The correctness of the prediction depends on whether the centroid distance between the predicted target and the ground truth is less than 3 pixels.

### 4.1.3 Optimization.

The algorithm is implemented in Pytorch, with Adaptive Gradient (AdaGrad) as the optimizer with the initial learning rate set to 0.05 and weight decay coefficient set to 0.0004. 2 NVIDIA A6000 GPU is used for training, with batch size set to 32. Dice loss [48] is adopted as the loss function. Training on SIRST and IRSTD-1k takes 800 epochs and 600 epochs respectively.

## 4.2 Quantitative Comparison

### 4.2.1 Accuracy Comparison.

We select some of the SOTA ISTD methods for comparison. As shown in Table 1, our MiM-ISTD generally achieves the best performances in terms of pixel-level metrics and object-level metrics on both datasets.

For the pixel-level metrics ( $IoU$ ,  $nIoU$ ), our method achieves the best performances, thanks to the further integration of inner Mamba blocks for local feature modelling. In this way, some distinguishable details that may get ignored by the outer Mamba block can get noticed, which promotes detection accuracy.

For the object-level metrics ( $P_d$ ,  $F_a$ ), how to reach a trade-off between  $P_d$  and  $F_a$  is challenging because the two metrics are mutually exclusive: higher  $P_d$  also increases the possibility of higher  $F_a$ . From Table 1, we can see that our method generally achieves the best object-level metrics results compared with other methods, especially detecting all the small targets ( $P_d = 100\%$ ) in the NUAA-SIRST test set. The result demonstrates that our MiM-ISTD can learn better representations to overcome missed detection and false alarms.



Table 2: Comparison of the model parameters (M), FLOPs (G), inference time (s) per image and GPU memory (M) per 4 batch size of different methods.

Method	Param(M) ↓	FLOPs(G) ↓	Inference(s) ↓	Memory(M) ↓	Avg nIoU ↑
ACM [16]	0.52	2.02	0.01	1121	64.73
DNANet [10]	4.7	56.34	0.15	10617	69.95
IAANet [20]	14.05	18.13	0.29	45724	66.45
RKformer [24]	29.00	24.73	0.08	-	69.54
ISNet [18]	1.09	122.55	0.05	15042	71.48
TCI-Former [11]	3.66	5.87	0.04	5160	73.77
MiM-ISTD	1.16	1.01	0.03	1774	74.01

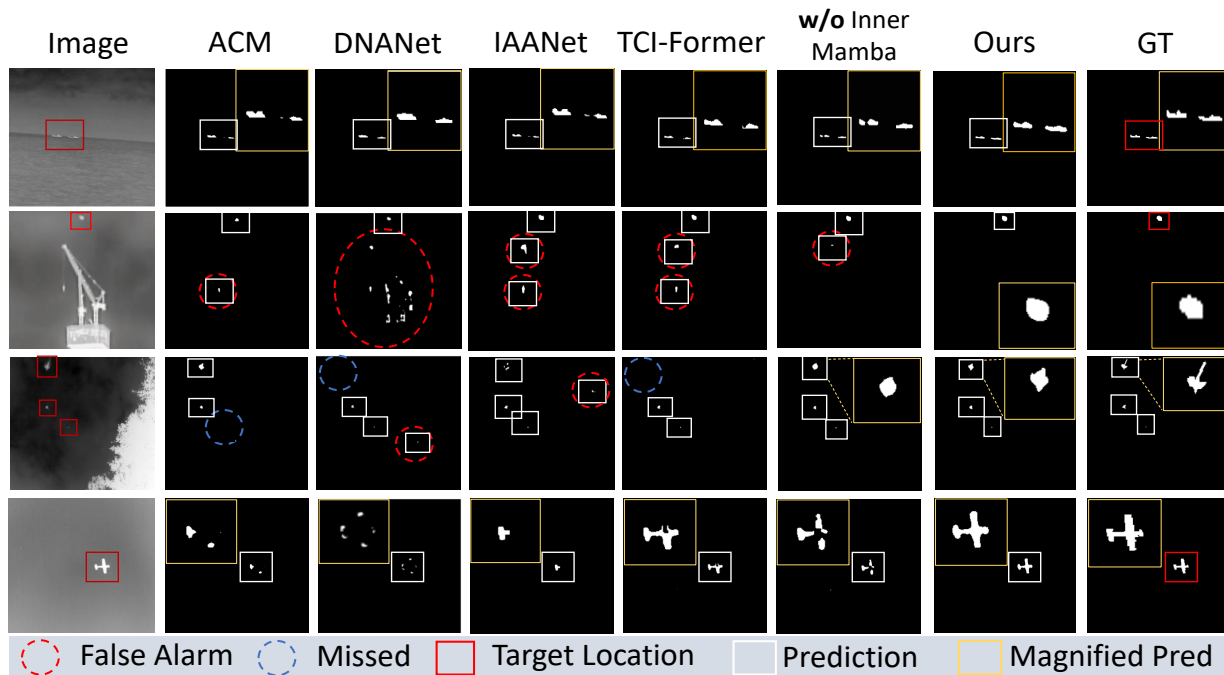


Figure 5: Visualization of predicted mask results.

#### 4.2.2 Efficiency Comparison.

We also compare the efficiency of different methods in terms of parameter number (M), FLOPs (G) and inference time (s) and GPU memory usage (M) during training on  $512 \times 512$  infrared image datasets, as shown in Table 2. Compared with other methods except ACM, our MiM-ISTD in general has significantly less parameters, GFLOPs, inference time and memory usage. This is because we adopt the efficient Mamba structure and also use a shared network to calculate the relations of each visual words in visual sentences so that the increased parameters and GFLOPs is negligible. Even compared with the most lightweight ISTD model ACM, our MiM-ISTD still has less GFLOPs and significantly higher accuracy. In addition, in higher resolution infrared image scenarios, we have compared in Fig. 1 that MiM-ISTD’s superiority of inference time and GPU memory usage will further be expanded while always maintaining a superior accuracy. Generally, MiM-ISTD reaches the best balance between efficiency and accuracy.

### 4.3 Visualization

#### 4.3.1 Visualization of Mask Results.

Visual results with closed-up views of different methods are shown in Fig. 5, where present methods more or less suffer from incomplete detection and missed detection. Compared with other SOTAs, our MiM-ISTD better curtails these cases and more completely detect the shapes of all small targets. This is because integrating an inner Mamba block assists our network to further exploit more local features, which promotes more refined detection of small targets. This

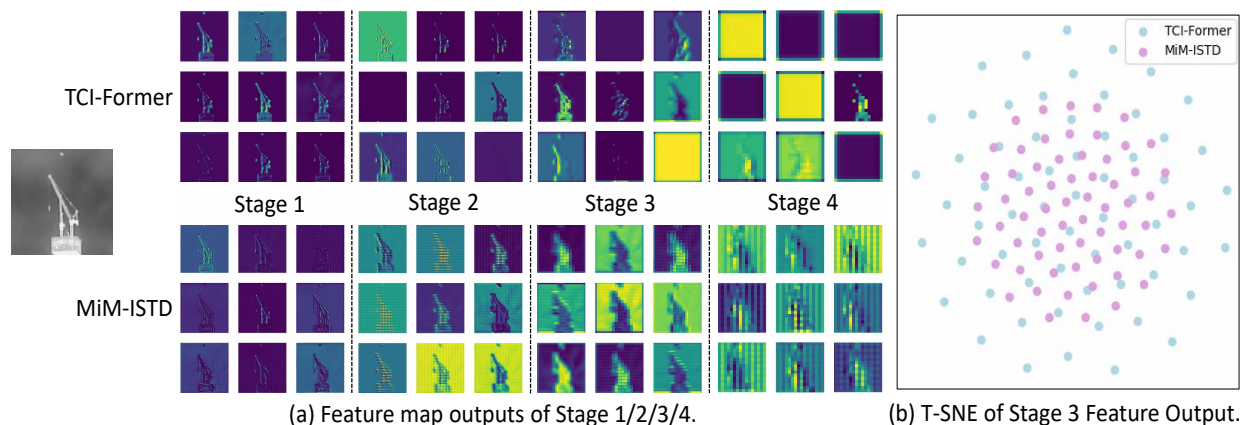


Figure 6: Visualization of the features of TCI-Former and MiM-ISTD.

Table 3: Ablation study of each module on NUAA-SIRST.

No.	Method	NUAA-SIRST			
		IoU $\uparrow$	nIoU $\uparrow$	Pd $\uparrow$	Fa $\downarrow$
#1	Baseline	76.33	73.60	98.17	8.125
#2	Inner Mamba $\rightarrow$ Conv	78.47	76.26	99.15	5.014
#3	Ours	<b>80.80</b>	<b>80.20</b>	<b>100</b>	<b>2.179</b>

can also be proved by comparing MiM-ISTD visual results with the "no inner Mamba" visual results, where abandoning inner Mamba brings worse detection performances.

### 4.3.2 Visualization of Feature Maps.

We visualize the learned features of TCI-Former and MiM-ISTD to further understand the effect of the proposed method. The feature maps are formed by reshaping the patch embeddings according to their spatial positions. The feature map outputs of stage 1, 2, 3 and 4 are shown in Figure 6 (a) where 9 feature map channels are randomly sampled for each of these outputs. In MiM-ISTD, the local information are better preserved in deeper layers compared to TCI-Former. Also, MiM-ISTD has higher feature consistency among each channels than TCI-Former, meaning that the features extracted by MiM-ISTD are more focused on the target. These benefits owe to the introduction of inner Mamba block to further model local features. We additionally visualize all the 64 channels of the stage 3 feature output using t-SNE [49] in Figure 6 (b) to demonstrate our analysis. We observe that the features of MiM-ISTD are more concentrated, exhibiting stronger discriminative power.

Table 4: Ablation study of the granularity of patch division on NUAA-SIRST.

No.	Method	NUAA-SIRST			
		IoU $\uparrow$	nIoU $\uparrow$	Pd $\uparrow$	Fa $\downarrow$
#1	Visual Word $\rightarrow 1 \times 1$	78.71	76.43	99.12	5.965
#2	Visual Word $\rightarrow 4 \times 4$	79.50	77.68	100	2.980
#3	Visual Sentence $\rightarrow H/4 \times W/4$	79.67	78.04	100	3.685
#4	Visual Sentence $\rightarrow H/16 \times W/16$	69.32	67.58	93.52	22.21
#5	Ours (VW $\rightarrow 2 \times 2$ , VS $\rightarrow H/8 \times W/8$ )	<b>80.80</b>	<b>80.20</b>	<b>100</b>	<b>2.179</b>

## 4.4 Ablation study

### 4.4.1 Ablation study of Each Module.

The ablation study of each module is shown in Table 3. Our baseline (No.#1) uses the visual Mamba [28] encoder as our encoder with descending spatial resolutions, where no inner Mamba block is employed. We also replace the inner Mamba block of our MiM-ISTD with the standard convolution, batch normalization and activation operations (No.#2) to examine the effect of our inner Mamba block. We find that our present setting brings the best results, because convolution typically focus on local information, while the inner Mamba block can capture complex spatial relationships and integrate multi-directional information to have a more delicate perception and identification of small targets.

### 4.4.2 Ablation Study of the Granularity of Patch Division.

To explore the impact of information contained in each visual word produced by the convolutional stem, we adjust the representation granularity of sub-patches so that each visual word corresponds to a  $1 \times 1$  (No.#1) or  $4 \times 4$  (No.#2) pixel region in the original image, in contrast to  $2 \times 2$  of our present setting. We also change the initial spatial shape of visual sentence from  $\frac{H}{8} \times \frac{W}{8}$  to  $\frac{H}{4} \times \frac{W}{4}$  (No.#3) and  $\frac{H}{16} \times \frac{W}{16}$  (No.#4) to ablate the effect of visual sentence granularity. We can observe that too large or too small division granularity cannot bring the most ideal performance. We adopt the configuration that demonstrates the best performance in our present setting.

## 5 Conclusion

In this paper, we propose a Mamba-in-Mamba (MiM-ISTD) structure for efficient ISTD. We uniformly divide the image into patches as visual sentences, and further split each patch to multiple smaller sub-patches as visual words. We devise a pure Mamba-based MiM hierarchical encoder that encompasses stacked MiM blocks. Each MiM block contains an outer Mamba block to process the sentence embeddings and an inner Mamba block to model the relation among word embeddings. The visual word embeddings are added to the visual sentence embedding after a linear projection. Experiments show that our method can achieve more efficient modelling of both local and global information.

## References

- [1] Mingjing Zhao, Wei Li, Lu Li, Pengge Ma, Zhaoquan Cai, and Ran Tao. Three-order tensor creation and tucker decomposition for infrared small-target detection. *IEEE Transactions on Geoscience and Remote Sensing*, 60:1–16, 2021.
- [2] Hu Zhu, Shiming Liu, Lizhen Deng, Yansheng Li, and Fu Xiao. Infrared small target detection via low-rank tensor completion with top-hat regularization. *IEEE Transactions on Geoscience and Remote Sensing*, 58(2):1004–1016, 2019.
- [3] Xiangzhi Bai and Yanguang Bi. Derivative entropy-based contrast measure for infrared small-target detection. *IEEE Transactions on Geoscience and Remote Sensing*, 56(4):2452–2466, 2018.
- [4] Yang Sun, Jungang Yang, and Wei An. Infrared dim and small target detection via multiple subspace learning and spatial-temporal patch-tensor model. *IEEE Transactions on Geoscience and Remote Sensing*, 59(5):3737–3752, 2020.
- [5] Fereshteh Seyed Marvasti, Mohammad Reza Mosavi, and Mahdi Nasiri. Flying small target detection in ir images based on adaptive toggle operator. *IET Computer Vision*, 12(4):527–534, 2018.
- [6] Landan Zhang and Zhenming Peng. Infrared small target detection based on partial sum of the tensor nuclear norm. *Remote Sensing*, 11(4):382, 2019.
- [7] Jinhui Han, Sibang Liu, Gang Qin, Qian Zhao, Honghui Zhang, and Nana Li. A local contrast method combined with adaptive background estimation for infrared small target detection. *IEEE Geoscience and Remote Sensing Letters*, 16(9):1442–1446, 2019.
- [8] Jean-Francois Rivest and Roger Fortin. Detection of dim targets in digital infrared imagery by morphological image processing. *Optical Engineering*, 35(7):1886–1893, 1996.
- [9] CL Philip Chen, Hong Li, Yantao Wei, Tian Xia, and Yuan Yan Tang. A local contrast method for small infrared target detection. *IEEE transactions on geoscience and remote sensing*, 52(1):574–581, 2013.
- [10] Boyang Li, Chao Xiao, Longguang Wang, Yingqian Wang, Zaiping Lin, Miao Li, Wei An, and Yulan Guo. Dense nested attention network for infrared small target detection. *IEEE Transactions on Image Processing*, 2022.

- [11] Tianxiang Chen, Zhentao Tan, Qi Chu, Yue Wu, Bin Liu, and Nenghai Yu. Tci-former: Thermal conduction-inspired transformer for infrared small target detection. *arXiv preprint arXiv:2402.02046*, 2024.
- [12] Bin Zhao, Chunping Wang, Qiang Fu, and Zishuo Han. A novel pattern for infrared small target detection with generative adversarial network. *IEEE Transactions on Geoscience and Remote Sensing*, 59(5):4481–4492, 2020.
- [13] Tianxiang Chen, Qi Chu, Zhentao Tan, Bin Liu, and Nenghai Yu. Bauenet: Boundary-aware uncertainty enhanced network for infrared small target detection. In *ICASSP 2023-2023 IEEE International Conference on Acoustics, Speech and Signal Processing (ICASSP)*, pages 1–5. IEEE, 2023.
- [14] Yimian Dai, Yiquan Wu, Fei Zhou, and Kobus Barnard. Attentional local contrast networks for infrared small target detection. *IEEE Transactions on Geoscience and Remote Sensing*, 59(11):9813–9824, 2021.
- [15] Tianfang Zhang, Lei Li, Siying Cao, Tian Pu, and Zhenming Peng. Attention-guided pyramid context networks for detecting infrared small target under complex background. *IEEE Transactions on Aerospace and Electronic Systems*, 2023.
- [16] Yimian Dai, Yiquan Wu, Fei Zhou, and Kobus Barnard. Asymmetric contextual modulation for infrared small target detection. In *Proceedings of the IEEE/CVF Winter Conference on Applications of Computer Vision*, pages 950–959, 2021.
- [17] Huan Wang, Luping Zhou, and Lei Wang. Miss detection vs. false alarm: Adversarial learning for small object segmentation in infrared images. In *Proceedings of the IEEE/CVF International Conference on Computer Vision*, pages 8509–8518, 2019.
- [18] Mingjin Zhang, Rui Zhang, Yuxiang Yang, Haichen Bai, Jing Zhang, and Jie Guo. Isnet: Shape matters for infrared small target detection. In *Proceedings of the IEEE/CVF Conference on Computer Vision and Pattern Recognition*, pages 877–886, 2022.
- [19] Tianxiang Chen, Qi Chu, Zhentao Tan, Bin Liu, and Nenghai Yu. Abmnet: Coupling transformer with cnn based on adams-bashforth-moulton method for infrared small target detection. In *2023 IEEE International Conference on Multimedia and Expo (ICME)*, pages 1901–1906. IEEE, 2023.
- [20] Kewei Wang, Shuaiyuan Du, Chengxin Liu, and Zhiguo Cao. Interior attention-aware network for infrared small target detection. *IEEE Transactions on Geoscience and Remote Sensing*, 60:1–13, 2022.
- [21] Meibin Qi, Liu Liu, Shuo Zhuang, Yimin Liu, Kunyuan Li, Yanfang Yang, and Xiaohong Li. Ftc-net: Fusion of transformer and cnn features for infrared small target detection. *IEEE Journal of Selected Topics in Applied Earth Observations and Remote Sensing*, 15:8613–8623, 2022.
- [22] Tianxiang Chen, Qi Chu, Bin Liu, and Nenghai Yu. Fluid dynamics-inspired network for infrared small target detection. In *Proceedings of the Thirty-Second International Joint Conference on Artificial Intelligence*, pages 590–598, 2023.
- [23] Fangcen Liu, Chenqiang Gao, Fang Chen, Deyu Meng, Wangmeng Zuo, and Xinbo Gao. Infrared small-dim target detection with transformer under complex backgrounds. *arXiv preprint arXiv:2109.14379*, 2021.
- [24] Mingjin Zhang, Haichen Bai, Jing Zhang, Rui Zhang, Chaoyue Wang, Jie Guo, and Xinbo Gao. Rkformer: Runge-kutta transformer with random-connection attention for infrared small target detection. In *Proceedings of the 30th ACM International Conference on Multimedia*, pages 1730–1738, 2022.
- [25] Albert Gu and Tri Dao. Mamba: Linear-time sequence modeling with selective state spaces. *arXiv preprint arXiv:2312.00752*, 2023.
- [26] Albert Gu, Karan Goel, and Christopher Ré. Efficiently modeling long sequences with structured state spaces. *arXiv preprint arXiv:2111.00396*, 2021.
- [27] Jun Ma, Feifei Li, and Bo Wang. U-mamba: Enhancing long-range dependency for biomedical image segmentation. *arXiv preprint arXiv:2401.04722*, 2024.
- [28] Yue Liu, Yunjie Tian, Yuzhong Zhao, Hongtian Yu, Lingxi Xie, Yaowei Wang, Qixiang Ye, and Yunfan Liu. Vmamba: Visual state space model. *arXiv preprint arXiv:2401.10166*, 2024.
- [29] Zi Ye and Tianxiang Chen. P-mamba: Marrying perona malik diffusion with mamba for efficient pediatric echocardiographic left ventricular segmentation. *arXiv preprint arXiv:2402.08506*, 2024.
- [30] Kai Han, An Xiao, Enhua Wu, Jianyuan Guo, Chunjing Xu, and Yunhe Wang. Transformer in transformer. *Advances in Neural Information Processing Systems*, 34:15908–15919, 2021.
- [31] Mingjin Zhang, Rui Zhang, Jing Zhang, Jie Guo, Yunsong Li, and Xinbo Gao. Dim2clear network for infrared small target detection. *IEEE Transactions on Geoscience and Remote Sensing*, 61:1–14, 2023.

- [32] Mingjin Zhang, Ke Yue, Jing Zhang, Yunsong Li, and Xinbo Gao. Exploring feature compensation and cross-level correlation for infrared small target detection. In *Proceedings of the 30th ACM International Conference on Multimedia*, pages 1857–1865, 2022.
- [33] Gao Chen, Weihua Wang, and Sirui Tan. Irstformer: A hierarchical vision transformer for infrared small target detection. *Remote Sensing*, 14(14):3258, 2022.
- [34] Lianghai Zhu, Bencheng Liao, Qian Zhang, Xinlong Wang, Wenyu Liu, and Xinggang Wang. Vision mamba: Efficient visual representation learning with bidirectional state space model. *arXiv preprint arXiv:2401.09417*, 2024.
- [35] Jiacheng Ruan and Suncheng Xiang. Vm-unet: Vision mamba unet for medical image segmentation. *arXiv preprint arXiv:2402.02491*, 2024.
- [36] Ziyang Wang, Jian-Qing Zheng, Yichi Zhang, Ge Cui, and Lei Li. Mamba-unet: Unet-like pure visual mamba for medical image segmentation. *arXiv preprint arXiv:2402.05079*, 2024.
- [37] Zhaohu Xing, Tian Ye, Yijun Yang, Guang Liu, and Lei Zhu. Segmamba: Long-range sequential modeling mamba for 3d medical image segmentation. *arXiv preprint arXiv:2401.13560*, 2024.
- [38] Fabian Isensee, Paul F Jaeger, Simon AA Kohl, Jens Petersen, and Klaus H Maier-Hein. nnu-net: a self-configuring method for deep learning-based biomedical image segmentation. *Nature methods*, 18(2):203–211, 2021.
- [39] Hu Cao, Yueyue Wang, Joy Chen, Dongsheng Jiang, Xiaopeng Zhang, Qi Tian, and Manning Wang. Swin-unet: Unet-like pure transformer for medical image segmentation. In *European conference on computer vision*, pages 205–218. Springer, 2022.
- [40] Ali Hatamizadeh, Vishwesh Nath, Yucheng Tang, Dong Yang, Holger R Roth, and Daguang Xu. Swin unetr: Swin transformers for semantic segmentation of brain tumors in mri images. In *International MICCAI Brainlesion Workshop*, pages 272–284. Springer, 2021.
- [41] Jiarun Liu, Hao Yang, Hong-Yu Zhou, Yan Xi, Lequan Yu, Yizhou Yu, Yong Liang, Guangming Shi, Shaoting Zhang, Hairong Zheng, et al. Swin-umamba: Mamba-based unet with imagenet-based pretraining. *arXiv preprint arXiv:2402.03302*, 2024.
- [42] Ziyang Wang and Chao Ma. Weak-mamba-unet: Visual mamba makes cnn and vit work better for scribble-based medical image segmentation. *arXiv preprint arXiv:2402.10887*, 2024.
- [43] Ziyang Wang and Chao Ma. Semi-mamba-unet: Pixel-level contrastive cross-supervised visual mamba-based unet for semi-supervised medical image segmentation. *arXiv preprint arXiv:2402.07245*, 2024.
- [44] Yijun Yang, Zhaohu Xing, and Lei Zhu. Vivim: a video vision mamba for medical video object segmentation. *arXiv preprint arXiv:2401.14168*, 2024.
- [45] Ankit Gupta, Albert Gu, and Jonathan Berant. Diagonal state spaces are as effective as structured state spaces. *Advances in Neural Information Processing Systems*, 35:22982–22994, 2022.
- [46] Sergey Ioffe and Christian Szegedy. Batch normalization: Accelerating deep network training by reducing internal covariate shift. In *International conference on machine learning*, pages 448–456. pmlr, 2015.
- [47] Dan Hendrycks and Kevin Gimpel. Gaussian error linear units (gelus). *arXiv preprint arXiv:1606.08415*, 2016.
- [48] Carole H Sudre, Wenqi Li, Tom Vercauteren, Sebastien Ourselin, and M Jorge Cardoso. Generalised dice overlap as a deep learning loss function for highly unbalanced segmentations. In *Deep learning in medical image analysis and multimodal learning for clinical decision support*, pages 240–248. Springer, 2017.
- [49] Laurens Van der Maaten and Geoffrey Hinton. Visualizing data using t-sne. *Journal of machine learning research*, 9(11), 2008.